This is a preprint, the final version is subject to change, of the American Mineralogist (MSA)
Cite as Authors (Year) Title. American Mineralogist, in press.
DOI: https://doi.org/10.2138/am-2020-7246

REVISION 2

ESTABLISHING A PROTOCOL FOR THE SELECTION OF ZIRCON INCLUSIONS IN GARNET FOR RAMAN THERMOBAROMETRY

Nicola Campomenosi[1], Daniela Rubatto[2], Joerg Hermann[2], Boriana Mihailova[3], Marco Scambelluri[1], Matteo Alvaro[4]

[1] *Department of Earth Science, Environment & Life, University of Genoa, Corso Europa 26, 16132 Genoa, Italy*

[2] *Institute of Geological Sciences, University of Bern, Baltzerstrasse 1+3 3012 Bern, Switzerland*

[3] *Department of Earth Sciences, University of Hamburg, Grindelallee 48, D-20146 Hamburg, Germany*

[4] *Department of Earth and Environmental Sciences, University of Pavia, Via A. Ferrata, 1 27100 Pavia, Italy*

Abstract

The structural and chemical properties of zircon inclusions in garnet megablasts from the Dora Maira Massif (Western Alps, Italy) were characterised in detail using Charge Contrast imaging, Raman spectroscopy and Laser Ablation Inductively Coupled Plasma Mass Spectrometry. The aim of this work is to determine to what extent the degree of metamictization, metamorphic recrystallization, inherent structural heterogeneity, chemical composition and zoning, along with the elastic stress imposed by the host mineral, can influence the Raman peak position of the zircon inclusion and hence, the residual pressure estimated via Raman geo-barometry. We show and confirm that metamictization and inherent structural heterogeneity have a major influence in the Raman spectra of zircon in terms of peak position and peak width. We suggest that for spectral resolution of 2 cm^{-1} the peak width of the B_{1g} mode near 1008 cm^{-1} of reliable grains must be smaller than 5 cm^{-1}. The method can be applied to both inherited igneous and newly formed Alpine metamorphic crystals.

By coupling structural and chemical information, we demonstrate that there are no significant differences between the Raman spectra of zircon with oscillatory-zoned texture, formed during magmatic crystallization, and those formed by fluid-induced Alpine (re)crystallization. The discrimination between magmatic and metamorphic zircon based only on micro-textural constraints is not robust. Finally, our results allow establishing a protocol devoted to the selection of reliable buried zircon inclusions, relying only on Raman spectroscopic measurements, to use for elastic thermobarometry applications.

Keywords: Dora Maira Massif, elastic barometry, zircon, metamictization

Introduction

Zircon is one of the most common accessory minerals in various igneous, sedimentary and metamorphic rocks. Furthermore, due to its large stability field and its physical robustness, zircon often hosts UHP metamorphic minerals such as coesite and diamond (Parkinson and Katayama, 1999; Ye et al., 2000b; Hermann et al., 2001; Katayama and Maruyama, 2009). Zircon can be used for a wide range of applications, including U-Pb geochronology, and potential use as a host phase for the disposal of excess weapons-grade Pu, because of its capacity to incorporate radioactive elements, (e.g. Ewing et al., 1995). Further, radiation-damaged zircon has been successfully applied as a model system to elucidate the behaviour of partially ordered structures at high pressure and temperature conditions (e.g. Colombo et al., 1999; Binvignat et al. 2018).

A recent development in zircon petrology is its exploitation as a mineral inclusion in the frame of Raman elastic thermobarometry (Campomenosi et al., 2018; Zhong et al. 2019). The main idea is that the geochemical and isotopic information that can be obtained from zircon is complemented by elastic thermobarometry of zircon and its host in order to retrieve P-T-time-fluid-deformation paths of metamorphic and igneous rocks. For this new application, however, zircon composition and structural metamictization due to the decay of radioactive elements such as U and Th within its crystal structure

has to be taken into account, because the radiation-induced structural changes can lead to large variations in the Raman spectrum. Indeed, the Raman peaks of radiation-damaged crystals shift towards lower wavenumbers, while the peak width increases with respect to pristine crystals taken as reference (Rios et al. 2000; Colombo et al., 1999; Nasdala et al., 2001; Geisler and Pidgeon, 2002; Binvignat et al, 2018). In this regard, useful diagrams such as peak width (Γ), in terms of *full width at half maximum*, vs peak position of the major Raman peak near 1008 cm^{-1} (B_{1g} phonon mode related to antisymmetric SiO_4 stretching) can be exploited to recognize the zircon crystals whose Raman spectra is unaffected by metamictization processes and that can be safely used for elastic thermobarometry purposes (e.g. Zhong et al. 2019). However, even though the degree of metamictization is the main factor affecting the Raman spectra of zircon, it is not the only one. Cathodoluminescence (CL) studies of zircon internal zoning (e.g. Rubatto and Gebauer, 2000, Corfu et al. 2003) reveal that single crystals of zircon, particularly in metamorphic rocks, commonly show a complex internal chemical and structural heterogeneity at the micrometer-scale. Furthermore, variations in the Raman peak positions can be caused also by chemical substitution: a typical example is Hf replacing Zr at the dodecahedral crystallographic site (e.g. Hoskin and Rodgers, 1996).

To address these problems we have chosen a particularly well-known sample suite from the Dora Maira UHP unit (Western Alps, Italy), where garnet megablasts host abundant zircon inclusions. We report micrometer-scale structural and chemical information of partially exposed zircon crystals studied by complementary Raman spectroscopy, charge contrast (CC) imaging, and Laser Ablation Inductively Coupled Plasma Mass Spectrometry (LA-ICP-MS). The purpose is (i) to determine quantitatively how the structural and chemical heterogeneities of zircons can affect their Raman spectrum and (ii) to propose a best-practice protocol for the selection of zircon inclusions suitable for elastic thermobarometric estimations.

Sample description

We selected exposed and buried zircon inclusions in garnet megablasts from the UHP whiteschists of the Dora Maira Massif. The investigated samples come from the two major outcrops of the Brossasco-Isasca Unit (e.g. Chopin, 1984): Vallone Gilba and Vallone Martiniana close to the Case Fapina and Case Parigi localities, respectively. Several polished sections of about 350 microns in thickness have been prepared from three different garnet megablasts (up to 15-20 cm in size). Zircon crystals are included in garnet and kyanite and range in size from ~ 10 to 200 microns; they are either single, isolated crystals or clusters of two or more inclusions. The shape of the inclusions varies from rounded to elongated and almost idiomorphic with sharp corners and edges. Some of the zircon crystals also host mineral inclusions such as rutile, coesite, sheet silicates and apatite, in agreement with previous observations (e.g. Gautiez-Putallaz et al. 2016).

Previous results (Gebauer et al., 1997; Gautiez-Putallaz et al., 2016) suggested the existence of two main zircon generations that can coexist within the same crystal in these rocks. The first one records the crystallization of the Permian protolith (~275 Ma), while the second domain is Eocene in age (35.1 ±0.8 Ma) and related to metamorphism during the Alpine subduction. Chopin (1984) was the first to constrain this metamorphic event at UHP conditions by finding coesite inclusions within garnet. Optically single crystals of coesite inclusions have been found also in this study, especially within the garnet neoblasts (SiO_2 saturated whiteschists). Within the garnet megablasts, rare coesite inclusions have been found only at the external rim. More recent studies have constrained the metamorphic peak conditions in the diamond stability field at about 4 – 4.3 GPa and 730 – 750 °C (e.g. Hermann, 2003; Ferrando et al., 2009; Gautiez-Putallaz et al., 2016).

The selection of completely buried zircon inclusions follows the protocol given by Campomenosi et al. (2018) for elastic barometry applications (i.e. small, similar in size, non-fractured and isolated inclusions within the centre of a non-fractured host). On the other hand, the selection of the exposed grains (about 60% of the total number of zircon inclusions present in the samples) was based on criteria such as variable size of the inclusion and of the surrounding intact host (the *effective* host), exposure degree of the inclusions (optically estimated in terms of the ratio between the exposed

and buried inclusion surface) and presence of fractures or any other kind of discontinuity in both the host and the inclusion.

Analytical methods

Exposed zircon inclusions were investigated by CC imaging first and Raman spectroscopy later to obtain textural and structural information, and finally by LA-ICP-MS for the chemical composition.

CC images were acquired with a ZEISS EV050 scanning electron microscope at the Institute of Geological Sciences, University of Bern, at low vacuum conditions (18 Pa), 12 kV, a beam current of 100 mA and a working distance of 9.5 mm. CC images were obtained from well-polished, uncoated samples. It has been demonstrated that CC images correlate exactly to cathodoluminescence images and result from the complex interaction between the electron beam, the positive ions generated by electron-gas interactions in the chamber, a biased detector, and the sample (Griffin et al. 2000; Watt et al. 2000). Internal check in the Bern laboratory confirmed that CC images are identical to panchromatic cathodoluminescence images.

Raman measurements were collected with two different Horiba Jobin-Yvon spectrometers: a T64000 triple-monochromator system operating in a subtractive mode and an Explora_Plus single-monochromator spectrometer at the University of Hamburg and Genova, respectively. The first one was equipped with a symphony LN_2-cooled CCD detector, 1800-gr/mm holographic gratings, an Olympus BH-41 optical microscope and a Coherent Ar^+ laser, whereas the second with a Peltier-cooled CCD detector, a 2400 gr/mm grating, an Olympus BH-41 optical microscope, and Nd:YAG solid state laser. In both cases, using a slit width of 100 microns, the spectral resolution was approximately 2 cm^{-1} (determined using the photoluminescence line of Sm: SrB_4O_7 for the T64000 and a Ne lamp for the Explora_Plus spectrometers) and therefore apparatus corrections of the peak widths were not required (Nasdala et al. 2001). Sufficient acquisition times and a surface density of the laser power were used to avoid sample overheating during the Raman measurements (Zhong et

al. 2019). The instrumental accuracy in the peak position determination was about 0.35 cm^{-1} for the T64000 spectrometer and about 0.55 cm^{-1} for the Explora_Plus. These values refer to the half of the spectral pixel-pixel distance, which results from several instrumental factors, including the CCD detector array, groove density of gratings, and excitation-light wavelength.

However, both the instruments were manually calibrated to the silicon Raman peak at 520.5 cm^{-1} at each measurement session and the stability of the instrumental setup was double-checked measuring reference crystals every 4 hours. The resulting standard deviation in the determination of the silicon peak along different days of measurements was approximately 0.04 cm^{-1}. Furthermore, a crosscheck of the two data set measured with the two different spectrometers has been performed on several zircon grains in order to verify their consistency. Finally, the lateral spatial resolution of the two instruments is approximately 1 micron and the probed volume at the sample surface is of about 1 micron cube.

The Origin Lab-Pro 2018 software package was used for data evaluation. The collected spectra were baseline corrected for the continuum luminescence background when necessary, temperature-reduced to account for the Bose-Einstein occupation factor (Kuzmany, 2009), and normalized to the acquisition time (7 s). Peak positions, FWHMs, and integrated intensities were determined from fits with pseudo-Voigt functions (PV = (1 – q)·Lorentz + q·Gauss, q is the weight coefficient). The criterion for the maximum number of fitted peaks was $\Delta I < I/2$, where I and ΔI are the calculated magnitude and uncertainty of each peak intensity, respectively.

Trace elements analyses were obtained with an ASI-RESOlution 193 nm laser system coupled to an Agilent 7900 quadrupole Inductively Coupled Plasma mass spectrometer (ICPMS) at the Institute of Geological Sciences, University of Bern. The laser was tuned to a repetition rate of 5 Hz and an energy output of 4 mJ (corresponding to an HV of about 26-27 kV). The ICPMS was tuned for maximum sensitivity and minimum production of molecular species, maintaining ThO^+/Th^+ at < 0.2%. The spot size on the zircon crystal was 20 microns. Analyses were standardized to glass NIST 612 and zircon 91500 was run as secondary standard to monitor accuracy. Stoichiometric Si was

157 employed as internal standard for zircon (SiO_2: 31.6 wt%). Reproducibility and accuracy were within
158 10 % or less across all analysed elements. The data were reduced with the freeware Iolite (Paton et
159 al. 2011) and its data reduction scheme for trace elements (Woodhead et al. 2007).
160
161 **Results**
162 **Partially exposed zircon inclusions**
163 ***Charge Contrast (CC) imaging***
164 CC imaging of 64 inclusions from samples DM17-13 and DM17-49 (Martiniana locality) and
165 83 grains from samples DMG4-6 and DM17-35 (Gilba locality) shows a large variability in zircon
166 internal texture. By combining the data on various crystals, it was possible to recognize at least 4
167 major domains (Fig. 1): (i) a *dark* (i.e. low CC-emission) domain, commonly corresponding to the
168 crystal cores, (ii) an *oscillatory-zoned* domain (medium-high CC emission), which usually
169 corresponds to entire crystals or the core of elongated crystals and are further subdivided into
170 *oscillatory-dark* and *oscillatory-bright* domains based on CC emission, (iii) a transition (or
171 *undefined*) domain, whose appearance is between the darker and a brighter domains and without a
172 defined internal texture, and (iv) a *bright* domain (i.e. high CC-emission), which usually belongs to
173 the external rim of the crystals. About 70% of zircon inclusions from the Gilba locality show a more
174 elongated shape with, a typical oscillatory-zoned core surrounded by 1 or 2 thin brighter rims. On the
175 other hand, about 80% zircon inclusions from the Martiniana locality present more sub-idiomorphic
176 shape and more homogeneous internal texture. Furthermore, as already reported by Gautiez-Putallaz
177 et al. (2016) for zircon hosted in Si undersaturated whiteschists, some of the analysed inclusions in
178 Martiniana, where garnet is more abundant, display oscillatory dark domains.
179
180 ***Raman spectroscopy***
181 Zircon has tetragonal symmetry with space group $I4_1/amd$. According to group-theory
182 analysis, the optical phonons at the Brillouin-zone centre of zircon are (Kroumova et al., 2003):

183 $\Gamma_{opt} = 2A_{1g} + A_{1u} + A_{2g} + 3A_{2u} + 4B_{1g} + B_{1u} + B_{2g} + 2B_{2u} + 5E_g + 4E_u$

184 The A_{1g}, B_{1g}, B_{2g} and E_g modes are Raman-active and therefore a total of 12 Raman peaks can be
185 observed in the spectrum of a randomly oriented zircon. According to previous studies (Williams and
186 Knittel, 1993; Nasdala et al., 2001 Binvignat et al., 2018), both pressure and metamictization affect
187 most strongly the B_{1g} mode near 1008 cm^{-1}, originating from anti-symmetrical SiO_4 stretching. For
188 this reason, our discussion is mainly focused on this phonon mode.
189 The Raman spectroscopic analysis is based on 250 spectra collected from 60 zircon inclusions in
190 different CC domains. As an example, Figure 1 shows the variation of the internal SiO_4 antisymmetric
191 stretching mode (B_{1g}) near to 1008 cm^{-1} of representative zircon inclusions exhibiting heterogeneous
192 CC emission. Generally, dark CC domains correspond to Raman peak broadening and shift toward
193 lower wavenumbers when compared to those collected across brighter or oscillatory-zoned domains.
194 Furthermore, transition CC domains show transitional average features also for the Raman spectra.
195 A more quantitative evaluation of the structural state of zircon crystals can be done plotting the
196 relationship between the phonon wavenumber ω and the corresponding peak widht Γ (Geisler and
197 Pidgeon 2002; Zhong et al. 2019). The data measured on partially exposed zircon inclusions (Figure
198 2) show two different trends that correlate with the four different zircon domains (*bright, oscillatory-*
199 *zoned, undefined* and *dark)* .

200 - The first trend is characterized by $\omega < 1008$ cm^{-1}, 4.5 $cm^{-1} \leq \Gamma < 12$ cm^{-1}, and $\omega(\Gamma)$ with a
201 negative slope (inverse correlation). The data points on this trend mostly correspond to zircon
202 domains with dark and oscillatory-dark CC emission.
203 - The second trend, at higher wavenumbers, is characterized by 1008 $cm^{-1} < \omega < 1011$ cm^{-1}, 3.5
204 $cm^{-1} < \Gamma < 5.5$ cm^{-1}, and $\omega(\Gamma) \approx$ constant. This trend is mostly defined by zircon domains with
205 *bright* and *oscillatory(-brigh)* CC emission.

Note that, on average, *oscillatory-dark* domains display the largest Γ and lowest wavenumber with respect to *oscillatory-bright* domains. On the other hand, *undefined* domains are difficult to classify since they scatter over the entire data.

LA-ICP-MS

The different types of zircon domains also show differences in trace element composition. Table 1a-b reports representative major, minor and trace elements composition of analysed zircon crystal inclusions as determined by LA-ICP-MS with the associated CC-emission domains. Hf concentration is usually around 11000 µg/g and only few analyses show higher values up to 14000 µg/g. U content varies significantly between oscillatory-bright zoned, oscillatory-dark and dark CC domains, with the last showing, usually, the highest concentration (see for example DM17-35-3a-zrc10-p1 and p2 or even DM17-35-3a-zrc14-p3 and p2 in Table 1a). U contents vary from a few hundred µg/g in the bright domains in crystal cores or rims to 5000 µg/g for the darker domains and generally show an inverse relationship with CC emission, indicating that U suppresses luminescence (e.g. Rubatto and Gebauer 2000).

In line with previous REE datasets (e.g. Gautiez-Putallaz et al. 2016), zircon cores with oscillatory or convolute zoning have a steep HREE-enriched pattern with a pronounced negative Eu anomaly (e.g. Figure 3-C p1). This REE pattern is characteristic of conditions where plagioclase was present and garnet was absent, i.e during the crystallization of the granitic protholith in Permian times (e.g. Gautiez-Putallaz et al. 2016).

The rims and many crystals with oscillatory zoning have lower REE contents and a flat HREE pattern with no or weak Eu-anomaly (e.g. Figure 3). This REE pattern is diagnostic for zircons formed during prograde to peak metamorphism, where feldspar is no longer stable (e.g. Gautiez-Putallaz et al. 2016). The variable slope of the HREE patterns ranging from slightly positive to even negative (Figure 3-C) indicates zircon growth together with garnet, as both minerals compete for the HREE. Therefore a first distinction between pre-Alpine inherited igneous zircon and Alpine metamorphic

zircon can be obtained from the trace element analysis. Notably, a number of large crystals that display a fine oscillatory to sector zoning more or less surrounded by a dark or light rim present a depletion in HREE and remain rather constant across the entire grain (e.g. Figure 3-D, 3-E). This demonstrates that oscillatory zoning occurs also in Alpine metamorphic zircon and is not restricted to inherited igneous zircon, demonstrating that both CC and trace elements are required for the correct classification of the zircon.

Previous analyses on the same locality demonstrated that inherited zircon cores are ca. 275 Ma old and metamorphic rims are 35.1 ± 0.8 Ma old (Gebauer et al., 1997, Gauthiez-Putallaz et al. 2016). In our case, a rough estimate of the age can also be obtained from the LA-ICP-MS data, even if proper age standardisation and common Pb correction have not been performed. The $^{206}Pb/^{238}U$ values estimated in such a way are in general agreement with those obtained before on zircon from the same locality and correlate with the distinction made from the REE patterns (Gauthiez-Putallaz et al. 2016). This rough age estimate allows distinguishing between Alpine domains (usually lower U content and bright or oscillatory-bright CC domains) and pre-Alpine domains (higher U content and dark or oscillatory-zoned CC domains at the zircon cores) especially in cases where REE patterns might be ambiguous (see Table 2). Notably the large crystals with oscillatory-sector zoning and low HREE content are of Alpine age.

Assuming an age of 275 Ma for the pre-Alpine and 35 Ma for the Alpine domains (Gebauer et al., 1997, Gauthiez-Putallaz et al. 2016) and based on the measured U-Th composition of the zircon domains, their accumulation radiation doses D_a was calculated as follows (e.g. Nasdala et al., 2001):

$$D_\alpha = \frac{0.9928\, N_A c_U n_{238}}{10^6 m_{238}} \left(e^{\lambda_{238} t} - 1\right) + \frac{0.0072\, N_A c_U n_{235}}{10^6 m_{235}} \left(e^{\lambda_{235} t} - 1\right) + \frac{N_A c_{Th} n_{232}}{10^6 m_{232}} \left(e^{\lambda_{232} t} - 1\right) \quad (1)$$

where λ_n and m_n are, respectively, the nuclear decay constant and mass of the corresponding isotope (^{238}U, ^{235}U and ^{232}Th) (Steiger and Jaeger; 1977), the coefficient n represents the number of α decays per nucleus ($n_{238} = 8$, $n_{235} = 7$ and $n_{232} = 6$) and N_A is the Avogadro's number c_U and c_{Th} are the measured concentrations of U and Th respectively and t the time. Note that Equation 1 presumes a U

isotopic composition of 99,28% ^{238}U and 0.72% ^{235}U. The resulting D_a values are reported in Table 2.

Completely buried zircon inclusions

The Raman spectra collected on the completely buried zircon crystals have higher wavenumbers (from 1010 cm^{-1} up to 1013.5 cm^{-1}) with respect to the partially exposed grains, with a Γ mostly between 3.5 and 5.5 cm^{-1}. Only a few analyses reach values up to 6.5 cm^{-1} (Figure 4). The overlap between the two sets of inclusions is limited to about 10% of the analyses.

The data from the exposed and fully enclosed zircon inclusions can also be analysed in terms of the wavenumber difference ($\Delta\omega$) between the B_{1g} mode near 1008 cm^{-1} and the A_{1g} mode near 440 cm^{-1} rather than the *absolute* wavenumber. In this way, since the data were collected along different sessions of measurements, we can avoid eventual effects due to instrumental drift. As shown previously by William and Knittel (1992) and more recently by Binvignat et al. (2018) both phonon modes show an increase in the phonon wavenumber as the hydrostatic pressure increases. However, as reported from the same authors, the A_{1g} mode shows a weaker pressure dependence with respect to the B_{1g} mode and, therefore, to an increase of the pressure acting on the crystal should correspond an increase in the value of $\Delta\omega$ (Figure 5).

Discussion

Effect of minor and trace elements on zircon Raman shift

A large number of non-formula elements can be incorporated in the zircon crystal structure, however, most of them are usually far below 1 wt% (e.g. Hoskin and Schaltegger 2003), with the notable exception of Hf. Raman data measured on isomorphic series $ZrSiO_4$ – $HfSiO_4$, suggest that even if as much as 25% of all Zr ions are replaced by Hf the frequency variation of the main peaks does not exceed 3 cm^{-1} (Hoskin and Rodgers, 1996). Furthermore, Nasdala et al. (2002) suggested that positions and Γ of the main peaks in annealed, metamict gemstone-quality zircon, containing up to 6000 ppm of U and 16300 ppm of Hf, deviate less than 1 cm^{-1} from the data of pure well-crystalline

283 $ZrSiO_4$. Therefore, since our exposed zircon inclusions contain impurities and trace elements below
284 these values (maximum U content is 5060 ppm and maximum Hf content is 14570 ppm, see Table
285 1), the effect of chemical variations on zircon Raman spectra is negligible.

286 Zircon variation in HREE composition (i.e. depletion in the Alpine domains) has been
287 previously interpreted as the result of growth zoning during metamorphism in a fractionating bulk
288 composition where REE are largely incorporated in garnet (e.g. Gautiez-Putallaz et al., 2016). Indeed,
289 the garnet host shows a similar REE pattern along a core-to-rim line profile (e.g. Gautiez-Putallaz et
290 al. 2016), indicating equilibrium conditions with the associated zircon grains. The qualitative
291 $^{206}Pb/^{238}U$ measurements confirm that zircon crystals showing a flat HREE pattern throughout the
292 entire grain are completely metamorphic in origin. In this regard, it is important to note that, although
293 REE chemical zonation does not influence the main Raman scattering features, such as peak
294 broadening and position, it can give rise to heterogeneous photoluminescence, and hence to different
295 background levels of the Raman spectra collected from zones. Besides, depending on the excitation
296 laser wavelength, additional photoluminescence peaks may be observed next to the fundamental
297 Raman peaks of zircon.

298

299 **Metamorphic vs inherited zircon domains**

300 Charge contrast or cathodoluminesce imaging of metamorphic and inherited zircons usually
301 show notable differences in terms of the corresponding internal texture (e.g. Rubatto and Gebauer
302 2000, Corfu et al. 2003). Oscillatory-zoned grains have been chemically interpreted as the result of
303 alternating depletion and enrichment in trace elements (i.e. U and Y) during crystal growth at the
304 crystal-melt interface. On the other hand, bright domains at the rim of the crystals, usually show
305 higher and homogeneous CL-emission, presenting irregular shape that often overgrowths the pre-
306 existing crystals whose texture can sometime be evident as a relict (Rubatto and Gebauer, 2000). Our
307 results indicate that metamorphic zircon can also include dark, bright, oscillatory and undefined CC

domains. This observation warns against using internal zircon zoning alone for distinguishing magmatic versus metamorphic zircon.

As portrayed in Figure 2, bright and oscillatory-bright domains (yellow and blue spots, respectively), have the same Raman spectral features and define the "non-metamict" domain in the diagram (see details below). Therefore, despite their magmatic or metamorphic orgin, from a structural point of view, these two domains are effectively equivalent and there will be no difference in the calculated residual stress even if the two domains co-exist within the same crystal.

Finally, if we plot our data in a Γ of the B_{1g} mode near 1008 cm^{-1} vs D_α diagram, most of the Alpine domains fall within the broad interpolation line given by Nasdala et al. 2001 (Figure 6). Nasdala et al. (2001) interpreted the data plotting outside of such interpolation band as the possible effects of thermal annealing in the crystal. In our case, we interpret the few points outside the interpolation band as the result of possible partial annealing of inherited zircon cores (Permian and Caledonian in age) during the Alpine metamorphism.

Effect of metamictization and annealing on Raman shift

Previous studies have established that partial metamictization can have a major influence on zircon Raman spectra (e.g. Zhang et al., 2000; Geisler et al., 2001; Nasdala et al., 2001; Binvignat et al. 2018). In general, depending on the degree of metamictization, zircon crystals can show a significant Raman peak broadening and frequency shift toward lower wavenumbers with respect to pristine samples taken as reference. Furthermore, Geisler et al. (2001) pointed out the possible heterogeneous (step-evolution) effect that annealing could have on peak broadening and position.

Based on these considerations, the relationship between the peak width and the Raman shift (Figure 2) can be exploited as a discriminant between partially metamict/annealed crystals and pristine crystals, even when they are completely buried within their mineral host (see also Zhong et al. 2019). Indeed, differently to phonon wavenumber, variation in the Γ of a Raman peak is independent from minor amounts of stress (Binvignat et al., 2018) as those usually recorded in host-

inclusion systems. It follows that, when considering zircon inclusions, a buried partially metamict crystal should present Γ comparable to partially metamict crystals exposed at the surface and the same is valid for well-crystalline zircon grains. Therefore, we conclude that measurements with Γ greater than 5 cm^{-1} showing an inverse relationship with the Raman shift, represent partially metamict/annealed domains. On the other hand, domains with lower Γ (i.e. 3.5 – 5.0 cm^{-1}) and with no correlation with the Raman shift are associated to a non-metamict domain. In this regard, it is worth noting that also Alpine zircons with high U contents fall into the metamict domain.

Geisler and Pidgeon (2002) pointed out that possible annealing processes may influence both the Raman shift and the peak width, as well as the relationship between them during secondary geological processes. However, from their results, it is evident that such effects are critical for zircon with moderate to heavy levels of radiation damage (i.e. $\omega < 1004$ cm^{-1} and $\Gamma >$ than 11-12 cm^{-1}). In our case, the zircon inclusion displaying a negative slope result all with $\Gamma < 11$ cm^{-1} and $\omega > 1004$ cm^{-1}. This correlation can be tentatively interpreted as an indication that, as previously stated (e.g. Figure 6), annealing effects were negligible or absent in most of the samples over the relatively short geological evolution (280 or 35 Ma to present) and fast subduction metamorphism (Gebauer et al. 1997, Rubatto and Hermann 2001, Gauthiez Putallaz et al. 2016).

However, it is difficult to make a rigorous prediction of the effect of metamictization on the determination of the residual pressure of a buried inclusion. For zircon with Γ larger than 5 cm^{-1} there are at least two additional unknown variables:

- The reference wavenumber ω_0 of an equally metamict free crystal;
- The phonon mode compressibility $\beta = [1/\omega_0][d\omega/dP]$

Both variables are very sensitive to the accumulated radiation dose D_α (e.g. Binvignat et al., 2018). Unfortunately, the dispersion of our data in the established $\Gamma - D_\alpha$ trend is too large to give a reliable value of D_α and consequently of ω_0 and β for the purposes of Raman thermobarometry.

359 **Effect of zircon size on Raman shift for partially exposed inclusions**

360 For completely unstressed pristine crystals, the phonon wavenumber usually is expected not
361 to exceed the values of 1008.5 – 1009 cm^{-1} (see Binvignat et al., 2018; Geisler et al., 2001).
362 Nevertheless, our partially exposed grains, even considering only the non-metamict domain in Figure
363 2, show a larger variation (up to 1011 cm^{-1}).

364 As reported by Campomenosi et al. (2018), partially exposed inclusions can still preserve a
365 notable stress state in terms of Raman peak shift as function of the inclusion exposition degree and
366 size. In order to better clarify this issue, Figure 7 shows a Γ vs $\Delta\omega$ diagram of partially exposed
367 inclusions discriminating between grains with different size (< and > 50 microns). Note that, in this
368 case, we show only data from the exposed inclusions showing bright and or oscillatory-bright
369 domains at CC because only for such domains we can safely exclude other effects described above.
370 Data from inclusions of different size largely overlap. However, about 20% of the smaller inclusions
371 have a higher $\Delta\omega$ than the larger one (with one exclusion) and reach a $\Delta\omega$ of 572 cm^{-1} that are never
372 observed in the larger inclusions. This is in agreement with theoretical predictions (Mazzucchelli et
373 al., 2018) for which, within the same host, small inclusions, when partially exposed, tend to retain
374 more stress, due to the larger surface-to-volume ratio, i.e. larger impact of the host upon relatively
375 larger surface of the inclusion. On the other hand, small inclusions should exhibit less dispersion of
376 the degree of exposure. Hence, the quite large spread of our data is most probably due to the
377 superposition of both effects related to the inclusion size: the surface-to-volume ratio and the degree
378 of exposure.

379

380 **A new protocol for the selection of zircon inclusions in garnet for elastic barometry**

381 Based on the above considerations, we propose a simple protocol for selecting zircon inclusions
382 to get reliable residual pressure estimates for elastic barometry.

- Buried crystals must be isolated from other inclusions, section surfaces, host boundary, cracks and from any other kind of boundaries. This implies that thicker sections (i.e. 300 microns) are better (see also Campomenosi et al. 2018).
- At least 2-3 measurement spots for each crystal moving from core to rim should be performed: this enables detection of eventual structural heterogeneity within the crystal. For this pourpose, it is better to use a spectrometer with a confocal optical microscope in order to reach the best spatial resolution.
- An instrumental sepctral resultion equal or better than 2 cm^{-1} should be used and only those inclusions presenting a Γ of the B_{1g} mode near 1008 cm^{-1} smaller than 5 cm^{-1} should be considered. Note that this value represents the summation of the analytical uncertainty (i.e. instrumental spectral resolution) to the minimum value of about 3 cm^{-1} that has been measured on several grains by the two different spectrometers (see Figure 4).
- Only inclusions in which the phonon wave number and the Γ is constant across the entire crystal volume should be selected.
- If Γ is constant, but the phonon wavenumber changes across the crystal volume there could be effects due to the shape of the inclusion (Campomenosi et al. 2018). In this case it is reccomended to consider the measurement collected at the centre of the crystal to calculate the residual pressure of the inclusion.
- Partially exposed crystals should not be used as reference to calculate residual stress in the buried inclusions: they can be still under a notable residual stress state. It is reccomended using a completely free crystal or large exposed inclusions for which the residual stress state and the metamictization effects are negligible (see for example Figure 1-D).
- Whenever possible, a statistically significant amount of partially exposed inclusions should be selected in order to double check their textural complexity by CC or CL imaging and their chemistry. As an alternative, imaging and chemical checks should be performed on inclusions that have been exposed after the Raman measurements.

- Chemical and age measurements should be considered as important corollary information to reconstruct the petrogenesis of the zircon inclusions and the garnet host.

Implications

Zircon inclusions are difficult to manage correctly for elastic thermobarometry applications and a detailed characterization of the inclusions should be performed before extracting barometric data. In our systematic study the combination of structural and chemical information obtained by different analytical techniques on partially exposed zircon inclusions, allows to reliably predict the structural state of buried crystals for Raman spectroscopic measurements.

Our results provide a solid basis for the selection of reliable zircon inclusions to use for elastic thermobarometry applications. This methods, in combination with the already rich tool set that can be applied to zircon (e.g. Ti-in-zircon thermometry (Whatson et al., 2006), U-Pb geochronology, oxygen isotopes) will provide an even more detailed characterization of P-T-t-fluid and deformation hystory of metamorphic rocks.

Aknowledges

This work was financially supported by the European Research Council (ERC) under the European Union's Horizon 2020 research and innovation program grant agreements 714936 to M. Alvaro. Thanks are due to F. Piccoli and to A. Berger (University of Bern) for assistance in the LA-ICP-MS laboratory and the SEM laboratory, respectively, at the Institute of Earth Science of Bern and to N. Waeselmann for assistance in the laboratory of Raman spectroscopy at the University of Hamburg. We are grateful to D. Gatta for manuscript editing and to M. Cisneros and an anonymous reviewer for constructive comments. N. Campomenosi acknowledges the University of Genova for funding. D. Rubatto acknowledges the financial support of the Swiss National Science Foundation (project 166280).

435 **References**

436 Binvignat, F. A. P., Malcherek, T., Angel, R. J., Paulmann, C., Schlüter, J., and Mihailova, B.
437 (2018) Radiation-damaged zircon under high pressures. Physics and Chemistry of Minerals. 45, 981-
438 993

439

440 Campomenosi, N., Mazzucchelli, M. L., Mihailova, B., Scambelluri, M., Angel, R. J., Nestola,
441 F., Reali, A., and Alvaro, M. (2018) How geometry and anisotropy affect residual strain in host-
442 inclusion system: coupling experimental and numerical approaches. American Mineralogist, 103,
443 2032-2035.

444

445 Chopin, C. (1984) Coesite and pure pyrope in high-grade blueschists of the Western Alps: a
446 first record and some consequences. Contributions to Mineralogy and Petrology, 86, 107–118.

447

448 Colombo, M., Chrosch, J., and Salje, E. K. (1999) Annealing Metamict Zircon: A Powder X-
449 ray Diffraction Study of a Highly Defective Phase. Journal of the American Ceramic Society, 82(10),
450 2711-2716.

451

452 Corfu, F., Hanchar, J. M., Hoskin, P. W. O., and Kinny, P. (2003) Atlas of zircon textures.
453 Reviews in Mineralogy and Geochemistry 53:469-500

454

455 Ewing, R. C., Lutze, W., and Weber, W. J. (1995) Zircon: A host-phase for the disposal of
456 weapons plutonium. Journal of Materials Research, 10(2), 243-246.

457

458 Ferrando, S., Frezzotti, M. L., Petrelli, M., and Compagnoni, R. (2009) Metasomatism of
459 continental crust during subduction: the UHP whiteschists from the Southern Dora-Maira Massif
460 (Italian Western Alps). Journal of Metamorphic Geology, 27(9), 739-756.

Gauthiez-Putallaz, L., Rubatto, D., and Hermann, J. (2016) Dating prograde fluid pulses during subduction by in situ U–Pb and oxygen isotope analysis. Contributions to Mineralogy and Petrology, 171(2), 15.

Gebauer, D. H. P. S., Schertl, H. P., Brix, M., and Schreyer, W. (1997) 35 Ma old ultrahigh-pressure metamorphism and evidence for very rapid exhumation in the Dora Maira Massif, Western Alps. Lithos, 41(1-3), 5-24.

Geisler, T., Pidgeon, R. T., van Bronswijk, W., and Pleysier, R. (2001) Kinetics of thermal recovery and recrystallization of partially metamict zircon: a Raman spectroscopic study. European Journal of Mineralogy, 13(6), 1163-1176.

Geisler, T., and Pidgeon, R. T. (2002) Raman scattering from metamict zircon: comments on" Metamictisation of natural zircon: accumulation versus thermal annealing of radioactivity-induced damage" by Nasdala et al. 2001 (Contribution to Mineralogy and Petrology 141: 125-144). Contributions to Mineralogy and Petrology, 143(6), 750-755.

Griffin, B. J. (2000) Charge contrast imaging of material growth and defects in environmental scanning electron miscroscopy—linking electron emission and cathodoluminescence. Scanning 22(4):234-242.

Hermann, J. (2003) Experimental evidence for diamond-facies metamorphism in the Dora-Maira massif. Lithos, 70(3-4), 163-182.

Hermann, J., Rubatto, D., Korsakov, A., and Shatsky, V. S. (2001) Multiple zircon growth during fast exhumation of diamondiferous, deeply subducted continental crust (Kokchetav massif, Kazakhstan). Contribution to Mineralogy and Petrology 141:66-82.

Hoskin, P. W. O., and Rodgers, K. A. (1996) Raman spectral shift in the isomorphous series $(Zr_1$-xHfx)SiO_4. Eur. J. Solid State Inorganic Chemistry 33:1111-1121

Hoskin, P. W., and Schaltegger, U. (2003) The composition of zircon and igneous and metamorphic petrogenesis. In J. M. Hanchar and P. W. O. Hoskin, Eds., Zircon, 53, p. 427 467. Review in Mineralogy and Geochemistry, Mineralogical Society of America, Chantilly, Virginia

Katayama I., and Maruyama S. (2009) Inclusion study in zircon from ultrahigh-pressure metamorphic rocks in the Kokchetav massif: an excellent tracer of metamorphic history. Journal of the Geological Society 166:783-796.

Knittle, E., and Williams, Q. (1993) High-pressure Raman spectroscopy of $ZrSiO_4$: Observation of the zircon to scheelite transition at 300 K. American Mineralogist, 78(3-4), 245-252.

Kroumova, E., Aroyo, M. I., Perez-Mato, J. M., Kirov, A., Capillas, C., Ivantchev S., and Wondratschek, H. (2010) Bilbao Crystallographic Server : Useful Databases and Tools for Phase-Transition Studies. Phase Transitions, 76:1-2, 155-170

Kuzmany, H. (2009) Solid-State Spectroscopy. An introduction. Springer-Verlag, Berlin Heidelberg.

Mazzucchelli, M. L., Burnley, P., Angel, R. J., Morganti, S., Domeneghetti, M. C., Nestola, F., and Alvaro, M. (2018) Elastic geothermobarometry: Corrections for the geometry of the host-inclusion system. Geology, 46(3), 231-234.

Nasdala, L., Wenzel, M., Vavra, G., Irmer, G., Wenzel, T., and Kober, B. (2001) Metamictisation of natural zircon: accumulation versus thermal annealing of radioactivity-induced damage. Contributions to Mineralogy and Petrology, 141(2), 125-144.

Nasdala, L., Lengauer, C. L., Hanchar, J. M., Kronz, A., Wirth, R., Blanc, P., and Seydoux-Guillaume, A. M. (2002) Annealing radiation damage and the recovery of cathodoluminescence. Chemical Geology, 191(1-3), 121-140.

Parkinson C. D., and Katayama I. (1999) Present-day ultrahigh-pressure conditions of coesite inclusions in zircon and garnet: Evidence from laser Raman microspectroscopy. Geology 27(11):979-982.

Paton, C., Hellstrom, J., Paul, B., Woodhead, J., and Hergt, J. (2011) Iolite: freeware for the visualisation and processing of mass spectrometric data. Journal of Analytical Atomic Spectrometry. 26:2508–2518

Ríos, S., Salje, E. K., Zhang, M., and Ewing, R. C. (2000) Amorphization in zircon: evidence for direct impact damage. Journal of Physics: Condensed Matter, 12(11), 2401.

Rubatto, D., and Gebauer, D. (2000) Use of cathodoluminescence for U-Pb zircon dating by ion microprobe: some examples from the Western Alps. In: Pagel M, Barbin V, Blanc P, Ohnenstetter

D (eds) Cathodoluminescence in geosciences, vol. Springer, Berlin Heidelberg New York, pp 373-400.

Rubatto, D., and Hermann, J. (2001) Exhumation as fast as subduction?. Geology, 29(1), 3-6.

Rubatto, D., and Hermann, J. (2007) Zircon behaviour in deeply subducted rocks. Elements, 2007, 3.1: 31-35.

Ye K., Yao Y. P., Katayama I., Cong B. L., Wang Q. C., and Maruyama S. (2000b) Large areal extent of ultrahigh-pressure metamorphism in the Sulu ultrahigh-pressure terrane of East China: New implications from coesite and omphacite inclusions in zircon of granitic gneiss. Lithos 52: 157–164.

Watt, G. R., Kinny, P. D., and Griffin, B. J. (2000) Charge contrast imaging of geological materials in the environmental scanning electron microscope. American Mineralogist 85(11-12):1784-1794

Watson, E. B., Wark, D. A., and Thomas, J. B. (2006) Crystallization thermometers for zircon and rutile. Contribution to Mineralogy and Petrology 151:413-433

Woodhead, J. D., Hellstrom, J., Hergt, J. M., Greig, A., and Maas R. (2007) Isotopic and elemental imaging of geological materials by laser ablation inductively coupled plasma-mass spectrometry. Geostand Geoanal Res 31:331–343

Zhang, M., Salje, E. K., Capitani, G. C., Leroux, H., Clark, A. M., Schlüter, J., and Ewing, R. C. (2000) Annealing of-decay damage in zircon: a Raman spectroscopic study. Journal of Physics: Condensed Matter, 12(13), 3131.

Zhong, X., Andersen, N. H., Dabrowski, M., and Jamtveit, B. (2019) Zircon and quartz inclusions in garnet used for complementary Raman thermobarometry: application to the Holsnøy eclogite, Bergen Arcs, Western Norway. Contributions to Mineralogy and Petrology, 174(6), 50.

587 **Figure caption list**

588 **Figure 1**. Relationship between the CC emission domain and the corresponding Raman spectra (B_{1g}
589 mode near 1008 cm^{-1}) in partially exposed zircon inclusions. Samples DM17-35 are from Gilba
590 locality while sample DM17-13 comes from the Martiniana locality.

591

592 **Figure 2**. Γ vs Raman shift of the antisymmetric SiO_4 stretching B_{1g} mode near 1008 cm^{-1} of partially
593 exposed crystals with highlighted CC-emission domains.

594

595 **Figure 3**. REE pattern in selected partially exposed zircon inclusions. Colour coding follows that in
596 Figure 2: black = dark, green = oscillatory-dark, blue = oscillatory-bright, orange = bright, grey =
597 undefined. Yellow circles are scaled with respect the figure and are 20 micron across (laser spot)

598

599 **Figure 4**. Γ and Raman shift of partially exposed vs completely buried zircon inclusions

600

601 **Figure 5**. Γ of the B_{1g} mode near 1008 cm^{-1} and $\Delta\omega = \omega_{1008} - \omega_{440}$ of partially exposed vs selected
602 and completely buried zircon inclusions.

603

604 **Figure 6**. FWHM of the B_{1g} mode near 1008 cm^{-1} as function of the effect of increasing
605 metamictization in terms of accumulated radiation dose.

606

607 **Figure 7**. Γ of the B_{1g} mode near 1008 cm^{-1} vs $\Delta\omega = \omega_{1008} - \omega_{440}$ comparing small (< 50 microns)
608 and large (> 50 microns) partially exposed zircon inclusions. The spots refer only to bright and
609 oscillatory bright domains.

610

611

612

613

614

615

616

617

618

619

620

621

622

623

624

625

626

627

628

629

630

This is a preprint, the final version is subject to change, of the American Mineralogist (MSA)
Cite as Authors (Year) Title. American Mineralogist, in press.
DOI: https://doi.org/10.2138/am-2020-7246

631 **Table list**

Table 1a. Major, minor and trace elements (in µg/g) of zircon inclusions (spots are referred to Figure 3).

sample name	CC domain	Ti	Y	Nb	Hf	Pb	Th	U	sample name	CC domain	Ti	Y	Nb	Hf	Pb	Th	U
DM17-35-3A-zrc8-p1	Osc. dark	2.28	1639	3.16	10300	154	158	1436	DM17-35-1a-zrc6-p2	Osc. dark	14.3	720	8.31	14570	65.8	41.1	3147
DM17-35-3A-zrc8-p2	Osc. bright	4.70	2651	8.73	7710	390	793	1241	DM17-35-1a-zrc6-p3	dark	20.2	826	7.62	12610	77.1	32.8	2949
DM17-35-3A-zrc10-p1	Osc. bright	35.3	492	34.2	10880	10.0	84.9	378	DM17-35-1a-zrc3-p1	Osc. bright	13.3	204	1.63	12930	19.7	9.89	452
DM17-35-3A-zrc10-p2	dark	5.03	197	5.98	13690	52.4	2.61	2122	DM17-35-1a-zrc3-p2	dark	9.90	103.3	2.98	11690	73.7	7.82	3154
DM17-35-3A-zrc10-p3	bright	7.90	183	4.01	10840	24.3	6.85	883	DM17-35-1a-zrc3-p3	Osc. bright	13.1	161.8	3.09	12280	80.7	12.1	3700
DM17-35-3A-zrc14-p1	Osc. bright	2.91	850	1.94	12450	138	40.7	730	DM17-35-1a-zrc9-p1	Osc. bright	6.38	179.3	2.47	12190	43.7	16.8	1640
DM17-35-3A-zrc14-p2	Osc. dark	6.90	3140	8.05	10300	326	696	1900	DM17-35-1a-zrc10-p1	Osc. bright	10.8	587	2.42	11220	9.10	10.7	249.8
DM17-35-3A-zrc14-p3	Osc.bright	4.90	1820	4.50	11660	237	158	1320	DM17-35-1a-zrc10-p2	Osc. bright	790	536	8.53	10980	8.71	13.0	261
DM17-35-3A-zrc14-p4	Osc. bright	2.67	1353	1.42	8680	66.1	73.4	333	DM17-13-b-zrc13-p1	Osc. bright	17.0	1479	21.6	11960	31.1	51.5	1307
DM17-35-3A-zrc18-p1	Osc. bright	6.85	1850	1.64	9100	308	179.6	474	DM17-13-b-zrc13-p2	Osc. bright	11.8	1209	11.5	10820	22.5	26.6	755
DM17-35-3A-zrc13-p2	Osc. bright	1.69	920	3.05	9570	130	89.0	673	DM17-13-b-zrc15-p2	Osc bright	6.30	649	4.80	10180	16.9	11.5	604
DM17-35-3A-zrc13-p1	Osc. bright	1.79	1051	2.80	10960	154	87.0	828	DM17-13-b-zrc15-p3	Osc. bright	6.10	589	5.86	10310	9.37	7.11	346
DM17-35-3A-zrc13-p3	bright	3.04	1150	4.26	7070	242	336	635	DM17-13-b-zrc16-p1	Osc. bright	16.8	1817	13.7	10840	34.7	35.2	1342
DM17-35-5A-zrc2-p1	Osc. bright	10.3	211	5.86	11770	9.65	22.4	367	DM17-13-b-zrc16-p2	Osc. bright	8.50	383	3.96	11030	16.8	14.9	562
DM17-35-5A-zrc2-p2	Osc. bright	8.81	83.3	9.95	11190	17.6	34.3	695	DM17-13-b-zrc16-p3	Osc. dark	20.9	1504	29.9	10550	43.3	56.8	1538
DM17-35-5A-zrc2-p3	Osc. dark	8.30	83.4	8.75	11270	31.4	34.9	1208	DM17-13-b-zrc16-p4	Osc. bright	5.66	227.8	4.54	11550	10.3	18.5	435.3
DM17-35-5A-zrc2-p4	Osc. dark	4.60	58.5	3.10	11030	32.3	11.3	1148	DM17-13-c-zrc7-p1	Osc. bright	16.5	2140	2.44	10600	125	149	719
DM17-35-5A-zrc2-p5	bright	5.10	198	2.85	11170	28.6	7.17	1092	DM17-13-c-zrc7-p2	Osci. dark	10.2	1790	7.65	11900	21.1	13.2	950
DM17-35-5A-zrc3-p1	Osc. bright	2.02	930	0.76	9950	51.5	44.1	253	DM17-13-c-zrc7-p3	undefined	10.1	1982	12.5	12280	25.4	17.8	1037
DM17-35-5A-zrc14-p1	Osc. bright	48.3	1682	26.8	9768	8.94	87.1	380	DM17-13-c-zrc4-p1	bright	27.0	3250	24.3	12380	32.4	35.2	1335
DM17-35-5A-zrc14-p2	dark	10.1	490	5.49	11520	16.4	15.7	530	DM17-13-c-zrc4-p2	undefined	11.8	2100	13.6	11850	56.1	39.8	931
DM17-35-5A-zrc14-p3	bright	10.8	430	6.06	10840	3.80	12.3	112	DM17-13-c-zrc10-p1	dark	20.9	2680	33.7	11080	102	33.0	5060
DM17-35-5A-zrc14-p4	bright	22.5	632	20.1	11400	8.96	32.7	370	DM17-13-c-zrc10-p2	bright	7.30	582	4.56	11860	28.0	7.63	1175
DM17-35-5A-zrc14-p5	Osc. dark	7.10	262	6.38	12790	10.5	8.84	407	DM17-13-c-zrc10-p3	Osc. dark	10.7	1540	8.24	11480	46.2	6.67	2004

*Precision plus accuracy of measurements is within 10%

632

This is a preprint, the final version is subject to change, of the American Mineralogist (MSA)
Cite as Authors (Year) Title. American Mineralogist, in press.
DOI: https://doi.org/10.2138/am-2020-7246

Table 1b. REE composition (in µg/g) of zircon inclusions (spots are referred to Figure 3)

sample name	CC domain	La	Ce	Pr	Nd	Sm	Eu	Gd	Tb	Dy	Ho	Er	Tm	Yb	Lu
DM17-35-3A-zrc8-p1	Osc. dark	0.04	5.90	0.21	2.65	5.07	0.15	28.9	10.5	143	54.9	273	60.7	553	112
DM17-35-3A-zrc8-p2	Osc. bright	0.46	18.7	0.40	6.43	12.1	0.26	65.8	21.8	267	91.0	411	79.6	653	128
DM17-35-3A-zrc10-p1	Osc. bright	b.d.l.	2.80	0.04	1.06	6.80	2.23	70.5	16.0	86.2	12.3	29.5	4.80	38.9	6.95
DM17-35-3A-zrc10-p2	dark	b.d.l.	0.59	b.d.l.	b.d.l.	0.51	0.11	4.78	2.01	20.1	4.93	15.8	2.73	22.2	3.98
DM17-35-3A-zrc10-p3	bright	b.d.l.	1.03	b.d.l.	0.14	0.54	0.14	4.54	1.83	19.6	4.77	17.0	2.67	19.3	2.80
DM17-35-3A-zrc14-p1	Osc. bright	b.d.l.	0.44	b.d.l.	0.17	1.06	0.19	10.05	4.41	63.0	26.4	143	35.7	351	73.0
DM17-35-3A-zrc14-p2	Osc. dark	12.0	37.0	3.10	14.6	11.5	0.55	61.0	22.7	291	104	497	101	839	156
DM17-35-3A-zrc14-p3	Osc.bright	0.49	3.40	0.21	1.19	3.14	0.19	22.0	9.90	142	57.1	305	71.7	670	135
DM17-35-3A-zrc14-p4	Osc. bright	0.04	1.54	0.04	1.13	3.51	0.15	20.8	8.45	115	44.7	219	46.1	408	79.5
DM17-35-3A-zrc18-p1	Osc. bright	1.12	5.21	0.85	8.20	10.7	0.97	51.6	16.9	192	62.1	269	53.6	454	84.8
DM17-35-3A-zrc13-p2	Osc. bright	b.d.l.	2.78	b.d.l.	0.29	1.49	0.12	9.77	4.76	73.3	30.2	161	37.3	350	71.9
DM17-35-3A-zrc13-p1	Osc. bright	b.d.l.	2.38	0.02	0.33	1.08	0.10	9.02	4.55	75.7	32.9	182	43.8	424	88.1
DM17-35-3A-zrc13-p3	bright	0.34	14.1	0.17	1.78	3.15	0.73	16.5	6.16	85.0	34.4	185	44.1	442	97.0
DM17-35-5A-zrc2-p1	Osc. bright	0.08	1.08	0.04	0.42	3.30	1.36	53.7	10.8	48.2	5.31	11.1	1.39	10.0	1.69
DM17-35-5A-zrc2-p2	Osc. bright	b.d.l.	0.75	b.d.l.	0.34	4.74	1.41	43.7	6.35	22.2	2.26	4.55	0.61	5.21	0.90
DM17-35-5A-zrc2-p3	Osc. dark	b.d.l.	0.99	b.d.l.	0.12	3.47	1.13	34.8	5.44	19.9	2.26	4.60	0.61	5.82	1.03
DM17-35-5A-zrc2-p4	Osc. dark	b.d.l.	0.57	b.d.l.	b.d.l.	0.91	0.37	13.3	2.64	12.1	1.45	3.48	0.61	4.62	0.88
DM17-35-5A-zrc2-p5	bright	b.d.l.	0.81	b.d.l.	b.d.l.	0.62	0.14	5.83	1.92	20.3	5.27	18.7	3.33	23.5	3.37
DM17-35-5A-zrc3-p1	Osc. bright	0.06	1.27	0.11	0.78	2.50	0.07	14.1	5.45	76.9	30.7	154	33.6	301	59.3
DM17-35-5A-zrc14-p1	Osc. bright	b.d.l.	3.06	0.02	1.10	10.1	3.72	164	46.6	288	47.8	117	16.7	118	19.3
DM17-35-5A-zrc14-p2	dark	0.40	2.11	0.19	1.35	2.51	0.86	31.0	9.74	70.3	12.9	32.5	4.76	31.7	5.42
DM17-35-5A-zrc14-p3	bright	b.d.l.	0.75	b.d.l.	0.27	2.44	0.65	31.7	9.81	68.9	11.6	30.1	4.66	34.8	6.21
DM17-35-5A-zrc14-p4	bright	b.d.l.	1.89	0.04	0.68	4.14	1.39	54.2	15.9	104	16.4	40.5	5.53	38.8	6.39
DM17-35-5A-zrc14-p5	Osc. dark	b.d.l.	0.72	b.d.l.	0.10	1.19	0.40	16.3	5.58	38.4	6.47	16.4	2.28	15.6	2.60

*Precision plus accuracy of measurements is within 10%

633

634

This is a preprint, the final version is subject to change, of the American Mineralogist (MSA)
Cite as Authors (Year) Title. American Mineralogist, in press.
DOI: https://doi.org/10.2138/am-2020-7246

635

Table 1c. REE composition (in µg/g) of zircon inclusions (spots are referred to Figure 3)

sample name	CC domain	La	Ce	Pr	Nd	Sm	Eu	Gd	Tb	Dy	Ho	Er	Tm	Yb	Lu
DM17-35-1a-zrc6-p2	Osc. dark	b.d.l.	1.42	0.02	0.66	6.17	1.75	64.7	18.2	118	18.4	43.4	5.31	30.5	4.17
DM17-35-1a-zrc6-p3	dark	0.08	2.06	0.07	1.08	7.30	1.84	72.4	20.2	131	21.2	49.2	6.34	36.5	5.05
DM17-35-1a-zrc3-p1	Osc. bright	0.06	1.83	0.06	0.86	1.35	0.27	8.60	2.45	21.8	5.43	19.8	3.36	24.6	3.52
DM17-35-1a-zrc3-p2	dark	b.d.l.	0.45	b.d.l.	0.13	0.74	0.23	7.75	2.34	15.4	2.60	7.27	1.19	8.46	1.46
DM17-35-1a-zrc3-p3	Osc. bright	b.d.l.	0.95	0.02	0.26	1.50	0.44	14.4	4.10	25.8	4.42	12.0	2.04	14.0	2.42
DM17-35-1a-zrc9-p1	Osc. bright	b.d.l.	0.53	b.d.l.	0.19	1.40	0.46	16.1	4.63	27.3	4.51	12.9	2.03	14.5	2.48
DM17-35-1a-zrc10-p1	Osc. bright	b.d.l.	0.56	b.d.l.	0.23	3.06	0.93	38.1	11.7	89.1	18.0	51.8	7.30	47.6	7.10
DM17-35-1a-zrc10-p2	Osc. bright	0.05	0.70	b.d.l.	0.20	2.45	0.91	36.0	10.4	81.6	16.8	47.4	6.71	42.7	6.59
DM17-13-b-zrc13-p1	Osc. bright	b.d.l.	1.14	0.01	0.44	7.78	3.36	110	32.1	219	42.4	115	16.5	96.9	14.3
DM17-13-b-zrc13-p2	Osc. bright	b.d.l.	0.64	b.d.l.	0.40	5.57	2.46	86.6	25.6	177	35.2	95.6	14.4	85.9	12.7
DM17-13-b-zrc15-p2	Osc bright	b.d.l.	0.67	b.d.l.	0.12	2.26	1.08	39.2	11.2	90.3	18.9	58.5	9.16	62.8	10.9
DM17-13-b-zrc15-p3	Osc. bright	b.d.l.	0.44	b.d.l.	0.09	1.87	0.97	33.6	10.1	80.4	17.2	54.2	8.52	55.6	8.56
DM17-13-b-zrc16-p1	Osc. bright	b.d.l.	0.88	b.d.l.	0.58	9.34	4.24	147	40.6	288	54.3	149	21.4	133	19.4
DM17-13-b-zrc16-p2	Osc. bright	b.d.l.	0.41	b.d.l.	0.16	2.34	0.96	32.0	8.26	58.5	11.0	30.3	4.72	33.8	6.03
DM17-13-b-zrc16-p3	Osc. dark	b.d.l.	1.28	b.d.l.	0.34	7.11	3.05	116	33.2	233	44.0	116	16.2	99.6	13.2
DM17-13-b-zrc16-p4	Osc. bright	b.d.l.	0.35	b.d.l.	0.14	1.32	0.54	15.3	4.54	32.1	6.00	16.2	3.04	26.4	5.43
DM17-13-c-zrc7-p1	Osc. bright	0.84	3.40	0.31	2.32	5.24	0.18	31.2	13.0	175	69.7	334	71.6	647	122
DM17-13-c-zrc7-p2	Osci. dark	b.d.l.	0.57	b.d.l.	0.15	2.20	1.22	54.0	23.0	230	55.0	164	25.0	160	24.0
DM17-13-c-zrc7-p3	undefined	b.d.l.	0.73	b.d.l.	b.d.l.	3.23	1.36	54.2	24.5	250	63.5	197	30.1	210	32.9
DM17-13-c-zrc4-p1	bright	b.d.l.	1.64	b.d.l.	0.53	6.90	2.72	97.7	39.0	397	104	335	54.3	407	69.1
DM17-13-c-zrc4-p2	undefined	b.d.l.	1.21	b.d.l.	0.28	3.64	1.53	54.4	21.5	230	67.1	247	45.7	377	68.5
DM17-13-c-zrc10-p1	dark	b.d.l.	1.97	b.d.l.	0.47	6.10	2.69	90.3	33.8	310	84.0	326	64.0	536	94.8
DM17-13-c-zrc10-p2	bright	b.d.l.	0.35	b.d.l.	b.d.l.	0.95	0.44	18.9	7.34	69.3	19.0	74.4	14.6	126	23.0
DM17-13-c-zrc10-p3	Osc. dark	b.d.l.	0.62	b.d.l.	0.32	2.79	1.19	40.9	16.8	170	47.9	191	39.1	347	65.0

*Precision plus accuracy of measurements is within 10%

636

637

This is a preprint, the final version is subject to change, of the American Mineralogist (MSA)
Cite as Authors (Year) Title. American Mineralogist, in press.
DOI: https://doi.org/10.2138/am-2020-7246

Table 2. Indicative age and dose of partially exposed zircon inclusions (spots are referred to Figure 3)

sample name	CC domain	Indicative $^{206}Pb/^{238}U$	Indicative Age	D_alfa * (g/events)	Raman shift (cm^{-1})	FWHM (cm^{-1})
DM17-35-3A-zrc8-p1	Osc. dark	0.04	Permian	8.3E+17	1007.6	5.6
DM17-35-3A-zrc8-p2	Osc. bright	0.08	Caledonian	2.2E+18	1008.0	3.4
DM17-35-3A-zrc10-p1	Osc. bright	0.01	Alpine	5.3E+16	1007.9	3.9
DM17-35-3A-zrc10-p2	dark	0.01	Alpine	2.6E+17	1006.7	5.3
DM17-35-3A-zrc10-p3	bright	0.01	Alpine	1.2E+17	1007.9	3.6
DM17-35-5A-zrc2-p1	Osc. bright	0.01	Alpine	4.9E+16	1009.1	3.6
DM17-35-5A-zrc2-p4	Osc. dark	0.01	Alpine	1.6E+17	1008.0	4.5
DM17-35-5A-zrc2-p5	bright	0.01	Alpine	1.4E+17	1008.9	3.5
DM17-35-1A-zrc6-p2	Osc. dark	0.01	Alpine	3.3E+17	1008.9	3.5
DM17-35-1A-zrc6-p3	dark	0.01	Alpine	3.9E+17	1006.6	6.2
DM17-35-1A-zrc3-p2	dark	0.01	Alpine	3.7E+17	1006.3	5.7
DM17-35-1A-zrc3-p3	Osc. bright	0.01	Alpine	4.1E+17	1007.7	4.2
DM17-13-b-zrc13-p1	Osc. bright	0.01	Alpine	1.5E+17	1007.9	4.6
DM17-13-b-zrc13-p2	Osc. bright	0.01	Alpine	1.1E+17	1007.7	4.7
DM17-13-b-zrc15-p2	Osc bright	0.01	Alpine	8.6E+16	1008.3	4.5
DM17-13-b-zrc15-p3	Osc. bright	0.01	Alpine	4.7E+16	1008.3	4.0
DM17-13-b-zrc16-p1	Osc. bright	0.01	Alpine	1.7E+17	1007.9	5.1
DM17-13-b-zrc16-p2	Osc. bright	0.01	Alpine	8.5E+16	1008.2	4.0
DM17-13-b-zrc16-p3	Osc. dark	0.01	Alpine	2.2E+17	1007.3	5.6
DM17-13-b-zrc16-p4	Osc. bright	0.01	Alpine	5.3E+16	1008.3	3.6
DM17-13-c-zrc7-p1	Osc. bright	0.04	Permian	6.6E+17	1009.3	5.8
DM17-13-c-zrc7-p2	Osci. dark	0.01	Alpine	1.1E+17	1011.3	3.9
DM17-13-c-zrc7-p3	undefined	0.01	Alpine	1.3E+17	1010.2	4.3
DM17-13-c-zrc10-p1	dark	0.01	Alpine	5.2E+17	1006.2	10.6
DM17-13-c-zrc10-p2	bright	0.01	Alpine	1.4E+17	1008.3	3.3

DM17-13-c-zrc10-p3	Osc. dark	0.01	Alpine	2.3E+17	1007.4	5.0

639

This is a preprint, the final version is subject to change, of the American Mineralogist (MSA)
Cite as Authors (Year) Title. American Mineralogist, in press.
DOI: https://doi.org/10.2138/am-2020-7246

FIGURE 1

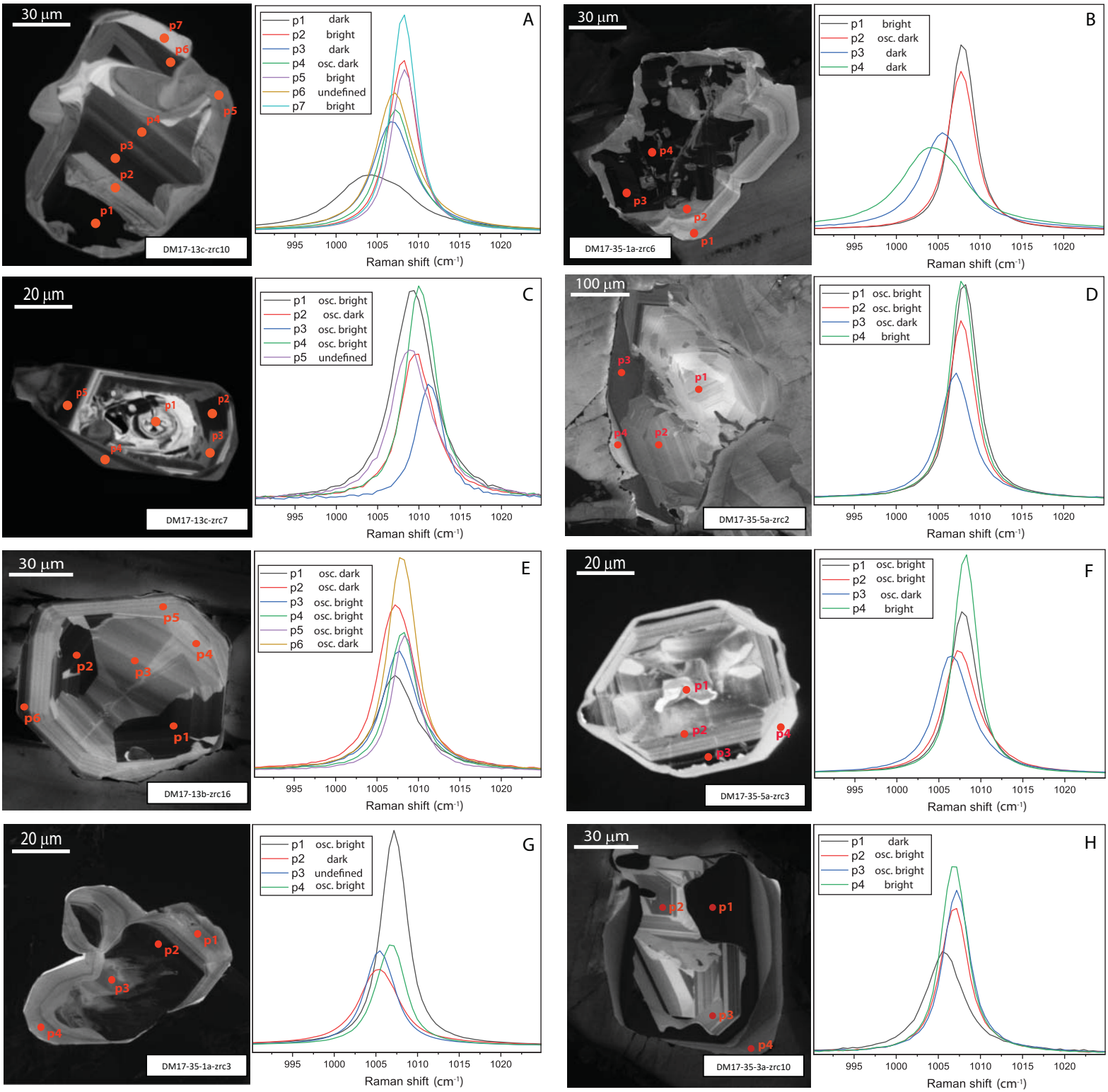

This is a preprint, the final version is subject to change, of the American Mineralogist (MSA)
Cite as Authors (Year) Title. American Mineralogist, in press.
DOI: https://doi.org/10.2138/am-2020-7246

FIGURE 2

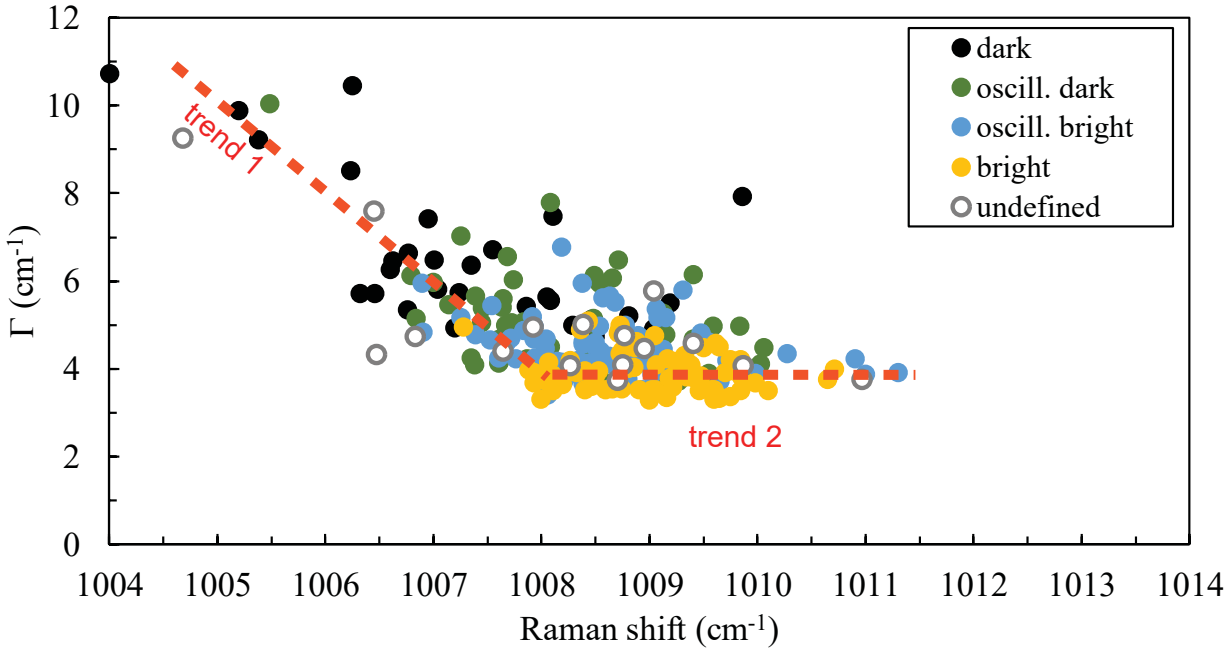

This is a preprint, the final version is subject to change, of the American Mineralogist (MSA)
Cite as Authors (Year) Title. American Mineralogist, in press.
DOI: https://doi.org/10.2138/am-2020-7246

FIGURE 3

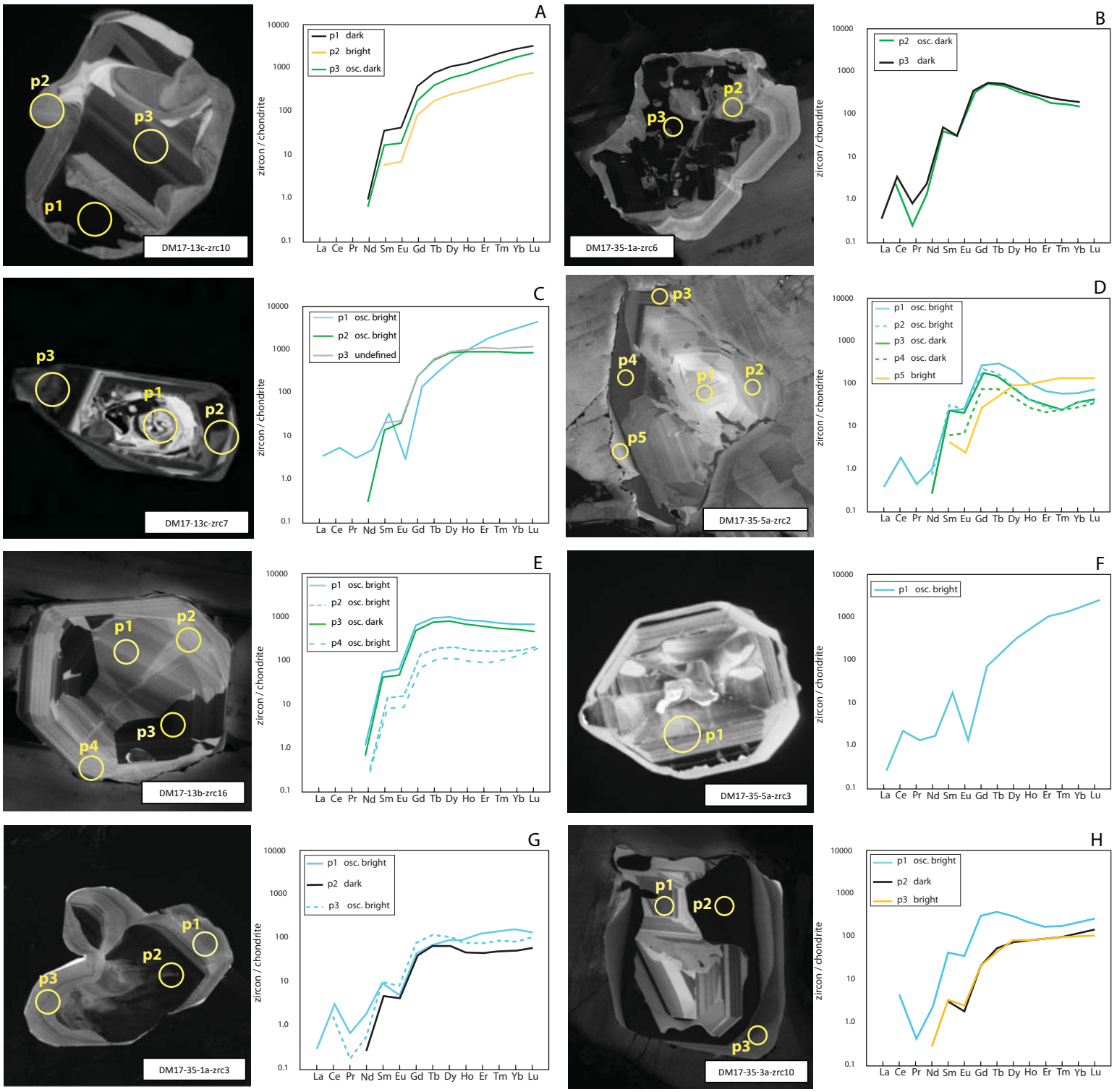

This is a preprint, the final version is subject to change, of the American Mineralogist (MSA)
Cite as Authors (Year) Title. American Mineralogist, in press.
DOI: https://doi.org/10.2138/am-2020-7246

FIGURE 4

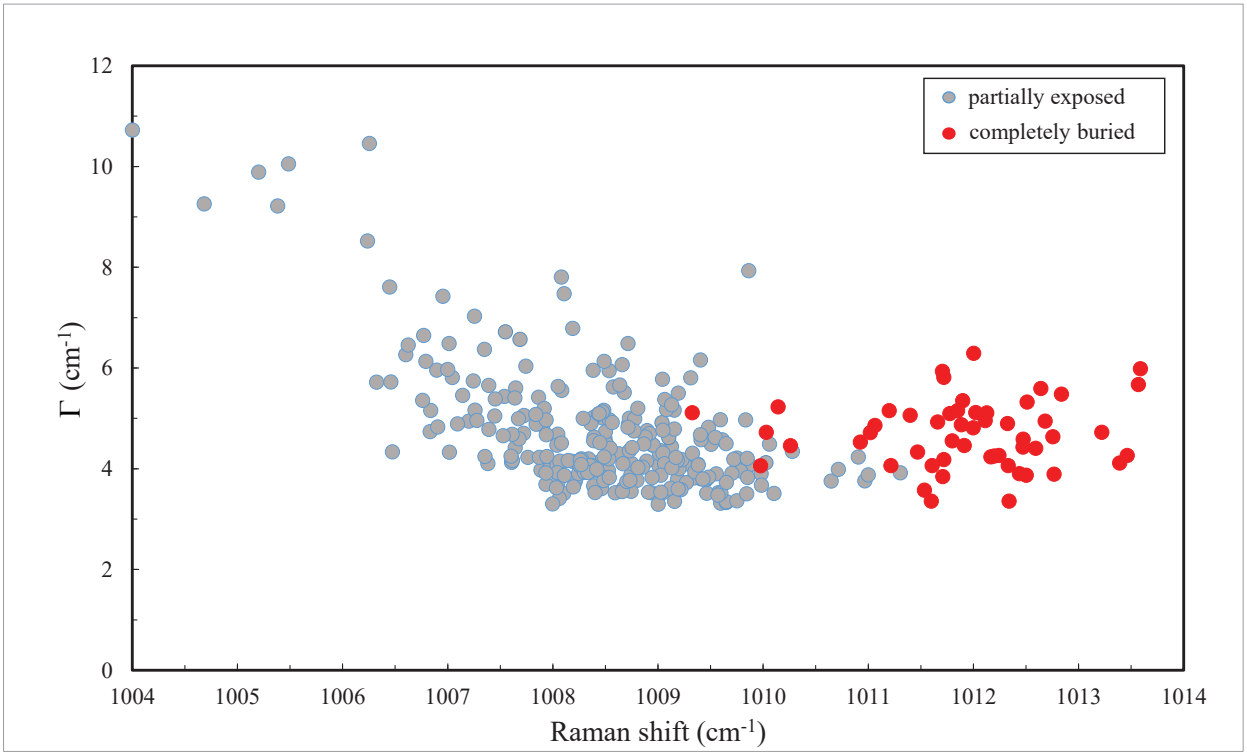

This is a preprint, the final version is subject to change, of the American Mineralogist (MSA)
Cite as Authors (Year) Title. American Mineralogist, in press.
DOI: https://doi.org/10.2138/am-2020-7246

FIGURE 5

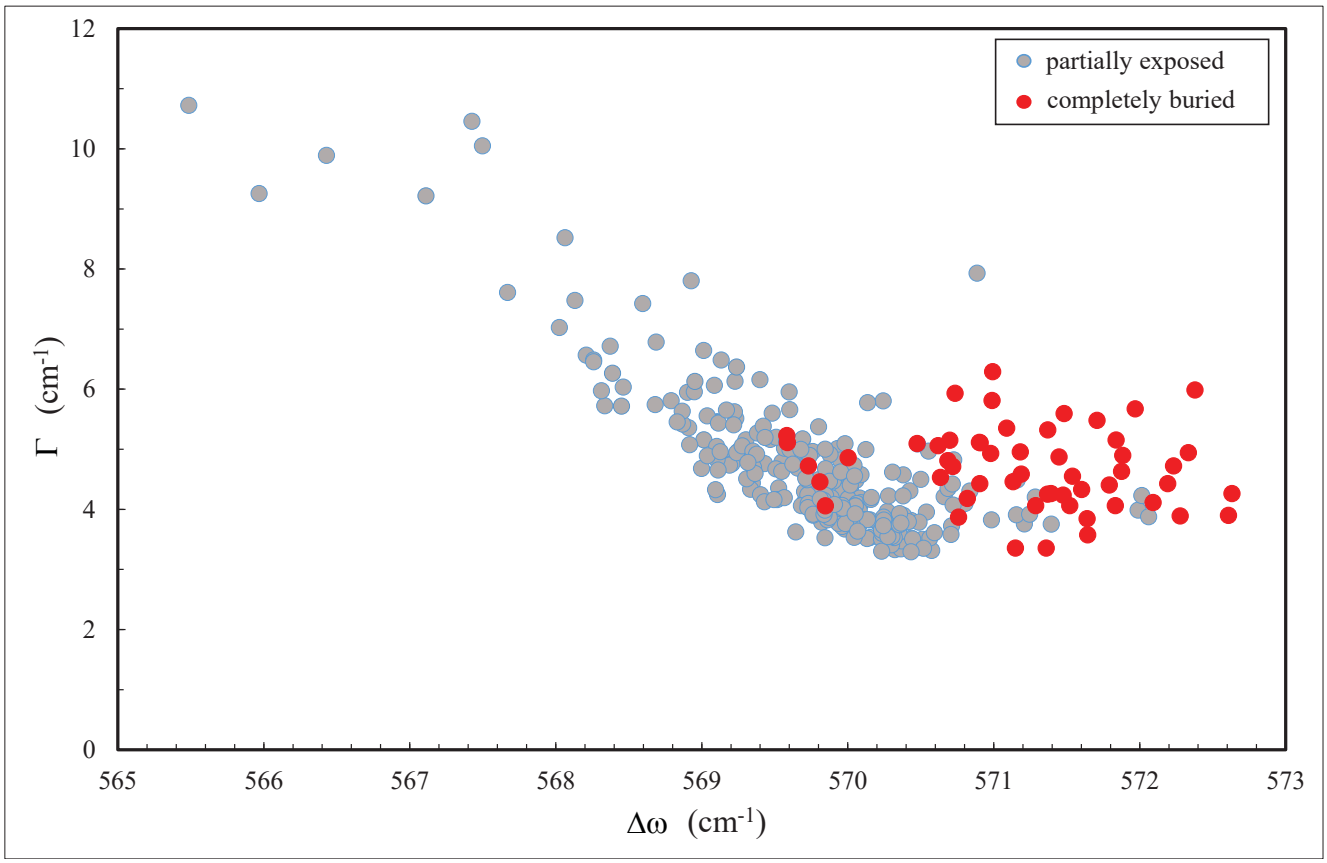

This is a preprint, the final version is subject to change, of the American Mineralogist (MSA)
Cite as Authors (Year) Title. American Mineralogist, in press.
DOI: https://doi.org/10.2138/am-2020-7246

FIGURE 6

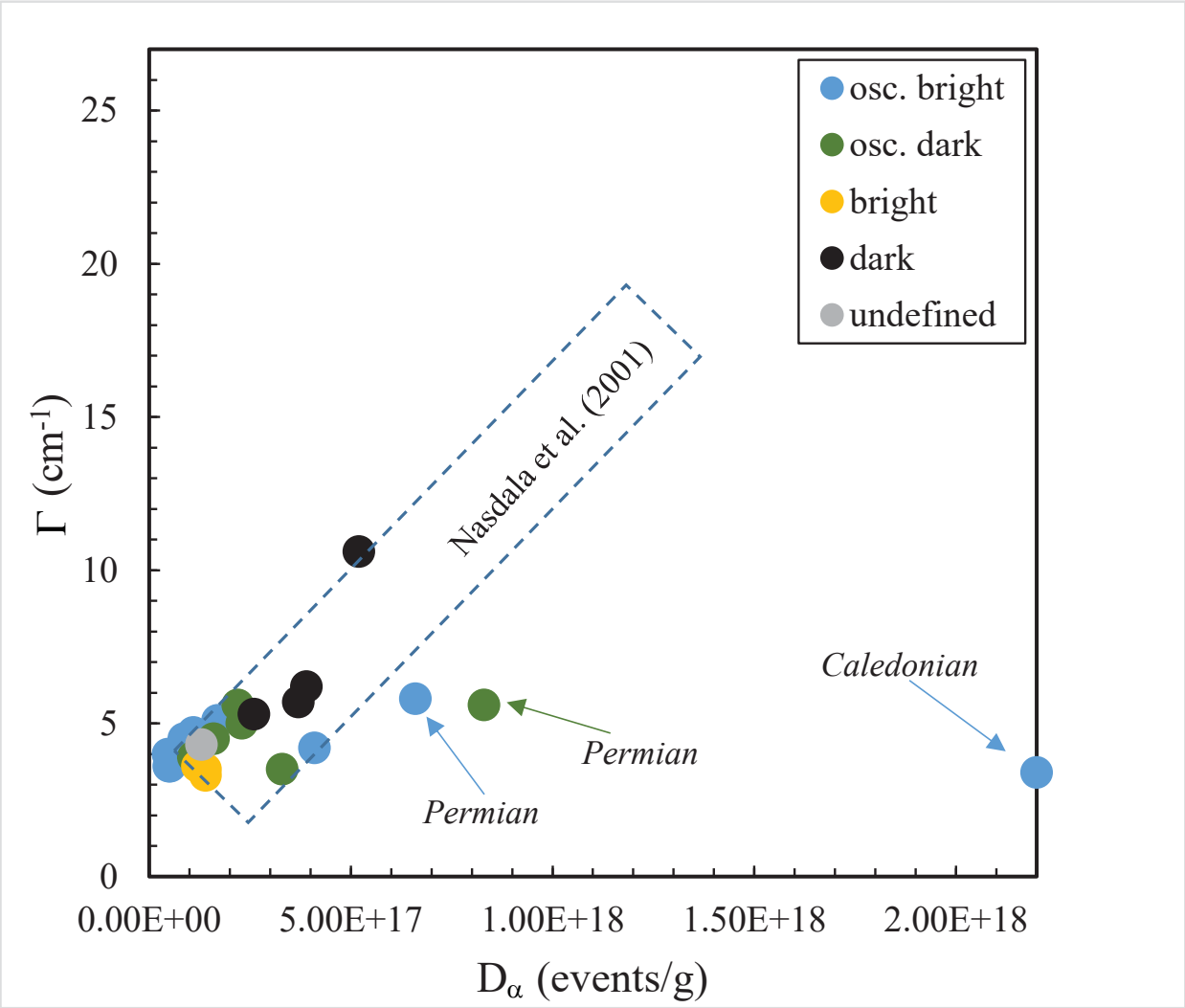

This is a preprint, the final version is subject to change, of the American Mineralogist (MSA)
Cite as Authors (Year) Title. American Mineralogist, in press.
DOI: https://doi.org/10.2138/am-2020-7246

FIGURE 7